JGR Space Physics

RESEARCH ARTICLE

10.1029/2022JA030444

Statistical Properties of Whistler-Mode Hiss Waves in the Inner Radiation Belt

Ling Yang[1,2], Liuyuan Li[1,2], Jinbin Cao[1,2], and Jiang Yu[3,4]

[1]School of Space and Environment, Beihang University, Beijing, China, [2]Key Laboratory of Space Environment Monitoring and Information Processing of MIIT, Beijing, China, [3]Planetary Environmental and Astrobiological Research Laboratory (PEARL), School of Atmospheric Sciences, Sun Yat-sen University, Zhuhai, China, [4]Key Laboratory of Tropical Atmosphere-Ocean System, Sun Yat-sen University, Ministry of Education, Zhuhai, China

Key Points:

- Middle-latitude hiss is equatorward propagating in the region of $L > 1.3$ but becomes poleward, azimuthal, or radial in the region of $L < 1.3$
- Amplitude of lower-band hiss (<600 Hz) is larger in the dayside high-L region and increases with enhanced substorm activities
- Amplitude of upper-band hiss (>600 Hz) is larger in the dayside low-L region and most nightside regions but has no substorm dependence

Correspondence to:

L. Li,
lyli_ssri@buaa.edu.cn

Citation:

Yang, L., Li, L., Cao, J., & Yu, J. (2022). Statistical properties of whistler-mode hiss waves in the inner radiation belt. *Journal of Geophysical Research: Space Physics*, *127*, e2022JA030444. https://doi.org/10.1029/2022JA030444

Received 9 MAR 2022
Accepted 10 MAY 2022

Author Contributions:

Conceptualization: Liuyuan Li
Data curation: Ling Yang, Jiang Yu
Formal analysis: Liuyuan Li
Funding acquisition: Liuyuan Li, Jinbin Cao
Investigation: Liuyuan Li
Methodology: Ling Yang, Liuyuan Li
Project Administration: Liuyuan Li, Jinbin Cao
Resources: Liuyuan Li
Software: Ling Yang, Jiang Yu
Validation: Ling Yang, Liuyuan Li, Jiang Yu
Visualization: Ling Yang
Writing – original draft: Ling Yang
Writing – review & editing: Liuyuan Li, Jinbin Cao

Abstract Using the Van Allen Probes A and B observations from 01 January 2013 to 28 February 2018, we surveyed statistically the occurrence rate, intensity, and propagation properties of hiss waves in the inner radiation belt ($1.1 < L \leq 2$). Like the outer plasmaspheric hiss ($L > 2$), the occurrence rate and amplitude of lower-band hiss (<600 Hz) are higher in the dayside high-L region ($L > 1.3$ and magnetic local time [MLT] = 6–20 hr) than the nightside (MLT ~ 20–6 hr) and increase with enhanced substorm activities (AE increases). Furthermore, their peak power spectral densities are located nearly in the same band (~200–500 Hz). The equatorward propagation of middle-latitude hiss suggests that the lower-band hiss waves in the inner radiation belt mostly originate from the outer plasmaspheric hiss at high latitudes. Although the outer plasmaspheric hiss is also a likely source of weak upper-band hiss (≥600 Hz) in the dayside high-L region ($L > 1.3$ and MLT = 6–20 hr), the intense upper-band hiss waves mostly appear in the dayside low-L region ($L < 1.3$) and most nightside regions. In the low-L region, the amplitude of the upper-band hiss has no obvious substorm dependence, and the average of its wave normal angles is comparable to that of lightning-generated whistlers reported in the past.

Plain Language Summary Whistler-mode hiss waves act like space sweepers, removing the high-energy radiation belt electrons and thereby creating a slot region relatively safe for satellites. Although ionospheric hiss ($L < 1.15$) and outer plasmaspheric hiss ($L > 2$) are frequently observed, most properties of hiss waves remain unclear in the inner radiation belt ($1.1 < L \leq 2$). Here, by surveying statistically the occurrence rate, intensity, and propagation properties of hiss waves observed by Van Allen Probes A and B in the inner belt region, we found that the amplitude of lower-band hiss (<600 Hz) is larger in the dayside high-L region ($L > 1.3$ and magnetic local time [MLT] = 6–20 hr) and increases with enhanced substorm activities, whereas that of upper-band hiss (≥600 Hz) is larger in the dayside low-L region ($L < 1.3$) and most nightside regions (MLT ~ 20–6 hr) but has no obvious substorm dependence. The averaged wave normal angle (WNA) in the upper band in the low-L region is comparable to that of lightning-generated whistlers. However, the WNA, peak power distribution, and strong substorm dependence of lower-band hiss are very similar to the outer plasmaspheric hiss.

1. Introduction

Whistler-mode hiss waves (tens of Hz to several kHz) mostly exist in the Earth's plasmasphere or plume and hence are known colloquially as "plasmaspheric hiss" (Meredith et al., 2004; Su et al., 2018; Thorne et al., 1973; Wang et al., 2020). When naturally generated hiss and man-made VLF waves (tens of kHz) appear in the same region, they can play complementary and catalytic roles in the loss of radiation belt electrons (L. Y. Li, Wang, et al., 2021). Hiss waves mainly remove relativistic electrons ($E > 0.5$ MeV) and thereby create a slot region relatively safe for satellites (Lyons & Thorne, 1973; Meredith et al., 2007; Yu et al., 2015, 2020).

Under different solar or geomagnetic activities, the space distribution variation of intense hiss waves effectively modifies the radial range of the slot region (L. Y. Li, Cao, et al., 2008; L. Y. Li, Yang, et al., 2019). Even though there are fast magnetosonic waves in the high-density plasmasphere, intense hiss waves are also able to remove most of the relativistic electrons (L. Y. Li, Yu, et al., 2017). The combined diffusions by the two kinds of waves cause different pitch angle distributions of energetic electrons under different ambient plasma densities (L. Y. Li, Yu, et al., 2022).

Past studies mainly investigated the amplitude of hiss waves in the region of $L > 1.4$ (Agapitov et al., 2013; W.; Li, Ma, et al., 2015; Meredith et al., 2018). Yu et al. (2017) showed the propagation characteristics of hiss waves in the outer plasmasphere ($L > 2$). Some low-earth orbit (LEO) satellites (e.g., Freja and DEMETER) also observed ionospheric hiss at the altitude of hundreds of km (Cao et al., 2005; Chen et al., 2017; Santolík & Parrot, 1999; Xia et al., 2019; Zhima et al., 2017). However, the hiss occurrence rate, propagation property, and frequency-spectral distribution remain unclear in most regions of the inner radiation belt ($1.1 < L \leq 2$). These unknowns add to the uncertainty about the source of the inner belt hiss waves.

Here, using the Van Allen Probes A and B observations from 01 January 2013 to 28 February 2018, we surveyed statistically the occurrence rate, intensity, and propagation properties of hiss waves in the entire inner belt region. Data and methodology are introduced in Section 2. Statistical results are presented in Section 3. The potential sources of the inner belt hiss waves in different bands are discussed in Section 4, and conclusions are summarized in Section 5.

2. Data and Methodology

Figure 1 displays two examples of whistler-mode hiss waves observed by Van Allen Probes A and B in the inner radiation belt ($1.1 < L \leq 2$) under different geomagnetic conditions. The 1-min averaged AE index comes from the OMNI database in the Coordinated Data Analysis Web. The power spectral densities (E_p and B_p) of electric and magnetic fields are measured by the Electric and Magnetic Field Instrument Suite and Integrated Science (EMFISIS) on board the Van Allen Probes. The EMFISIS can measure plasma waves from 10 Hz to 12 kHz in the inner magnetosphere ($L \sim 1.1$–6.5) (Kletzing et al., 2013). Wave normal angle (WNA) and polarization ellipticity are calculated with the singular value decomposition (SVD) method (Santolík et al., 2003). The polar angle (θ) of the Poynting vector is estimated with the magnetic spectral matrix (Santolík et al., 2010). MLAT is the magnetic latitude (in degrees), and MLT is the magnetic local time (in hours).

Whistler-mode hiss waves are right-handedly polarized (Ellipticity > 0.6), and their frequency (f) is above the gyrofrequency of local protons (f_{cp}). The power spectral densities (E_p and B_p) of hiss waves are significantly larger than the background values ($E_p \geq 5 \times 10^{-13}$ (V/m)^2/Hz and $B_p \geq 5 \times 10^{-8}$ nT^2/Hz) and they propagate nearly parallel to the background magnetic fields (WNA $\sim 10°$–$40°$). Except for sporadically vertical stripes above 600 Hz (Figures 1c and 1e), the power spectral densities of most hiss waves are continuous in the inner radiation belt; and their lowest frequency remains nearly invariant at different L-shells, which is different from the frequency dependence of locally excited waves on the cyclotron frequency of local plasma.

According to the criterions of right-handed polarization and effective wave intensity (ellipticity > 0.6, $E_p \geq 5 \times 10^{-13}$ (V/m)^2/Hz, and $B_p \geq 5 \times 10^{-8}$ nT^2/Hz), we picked out the inner belt hiss waves ($f_{cp} < f \leq 3000$ Hz) observed by Van Allen Probes A and B during the period from 1 January 2013 to 28 February 2018. The hiss wave amplitude (B_w) and WNA are calculated with the same methods as Yu et al. (2017). The radial distance ($L \sim 1.1$–2), magnetic latitude (MLAT $\sim -22.4°$–$18°$), and magnetic local time (MLT ~ 0–24 hr) of the selected hiss waves are divided into 40 grids, respectively. Finally, we obtained the average of hiss amplitude (B_w) and the medians of propagation angles (WNA and θ) in each statistical grid ([0.6 MLT $\times$ 0.025 L] [0.6 MLT and 1.01MLAT], or [0.025 L and 1.01MLAT]) under different geomagnetic (AE) conditions. AE index is an indicator of substorm intensity (L. Y. Li, Cao, et al., 2006, 2009; Li & Wang, 2018). AE ≤ 100 nT for quiet times; $100 <$ AE ≤ 300 nT for moderately active times; and AE > 300 nT for intensely active times.

3. Statistical Results

3.1. Hiss Occurrence Rate and Power Distribution in the Inner Radiation Belt

Figures 2a–2c displays the total number of times of Van Allen Probes A and B passing through the inner radiation belt during the statistical period (01 January 2013 to 28 February 2018). Figures 2d–2o displays the sample numbers and occurrence rates of hiss waves in the lower and upper bands under different geomagnetic (AE) conditions. The occurrence rate of hiss waves is the quotient of its sample number divided by the times of satellite passing in each statistical grid (0.6 MLT $\times$ 0.025 L). Although the orbit coverings of Van Allen Probes A and B are relatively uniform at different MLTs, the sample number and occurrence rate of lower-band hiss waves ($f_{cp} < f < 600$ Hz) are much larger on the dayside (MLT ~ 6–20 hr) than the nightside (MLT ~ 20–6 hr).

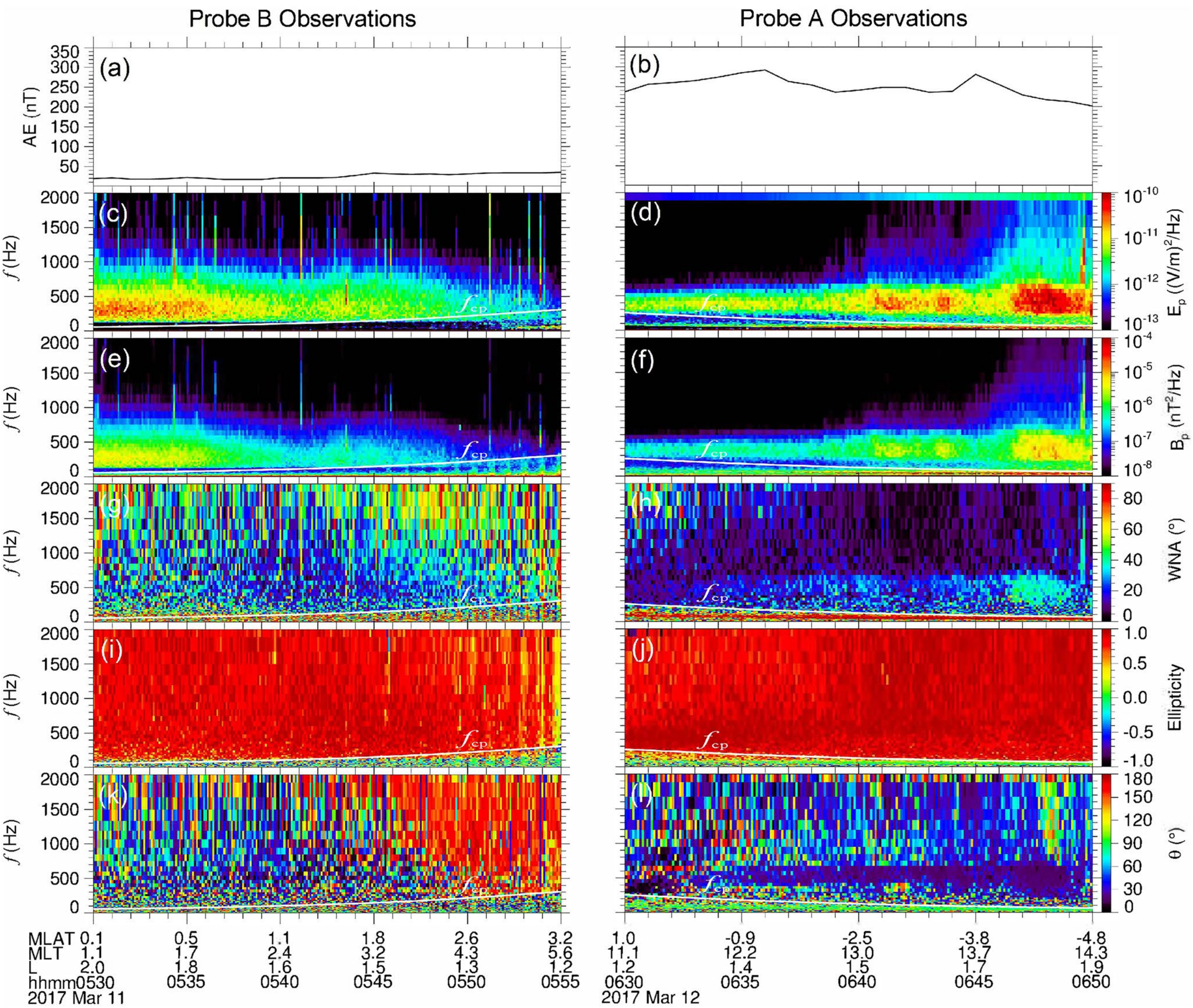

Figure 1. Whistler-mode hiss waves observed by Van Allen Probes A and B in the inner radiation belt ($1.1 < L \leq 2$). AE index is an indicator of substorm intensity. E_p and B_p are the power spectral densities of electric and magnetic fields, respectively. wave normal angle (WNA) is the wave normal angle, and Ellipticity is the polarization ellipticity. θ is the polar angle between the Poynting vector and background magnetic fields. White curve denotes the local proton gyrofrequency (f_{cp}).

Analogously, the sample number and occurrence rate of upper-band hiss waves ($f \geq 600$ Hz) have also significant day-night asymmetry in the high-L region ($L > 1.3$) of inner radiation belt (above the red dashed lines in Figures 2j–2o). In the dayside high-L region (between two vertical dashed lines), the occurrence rates of the inner belt hiss waves in the two bands gradually decrease as L decreases but slightly increase with enhanced substorm activities (AE increases). In contrast, the nightside hiss waves in the two bands have no obvious substorm dependence.

Figure 3 displays the hiss sample numbers and power spectral densities at different frequencies. The sample and power of hiss waves are mostly distributed in the lower band (covered by vertical shades), and their peak power is located between 200 and 500 Hz. The power spectral density (B_p) of the lower-band hiss (<600 Hz) increases as substorm activities are enhanced (AE increases). Under the same geomagnetic (AE) condition, the power spectral density of the lower-band hiss in the high-L region ($L > 1.3$) is larger than that near the inner boundary ($L < 1.3$). On the contrary, the power spectral density of the upper-band hiss (≥600 Hz) in the high-L region is less than that near the inner boundary, and their intensity (B_p) is nearly independent of substorm activities. The different

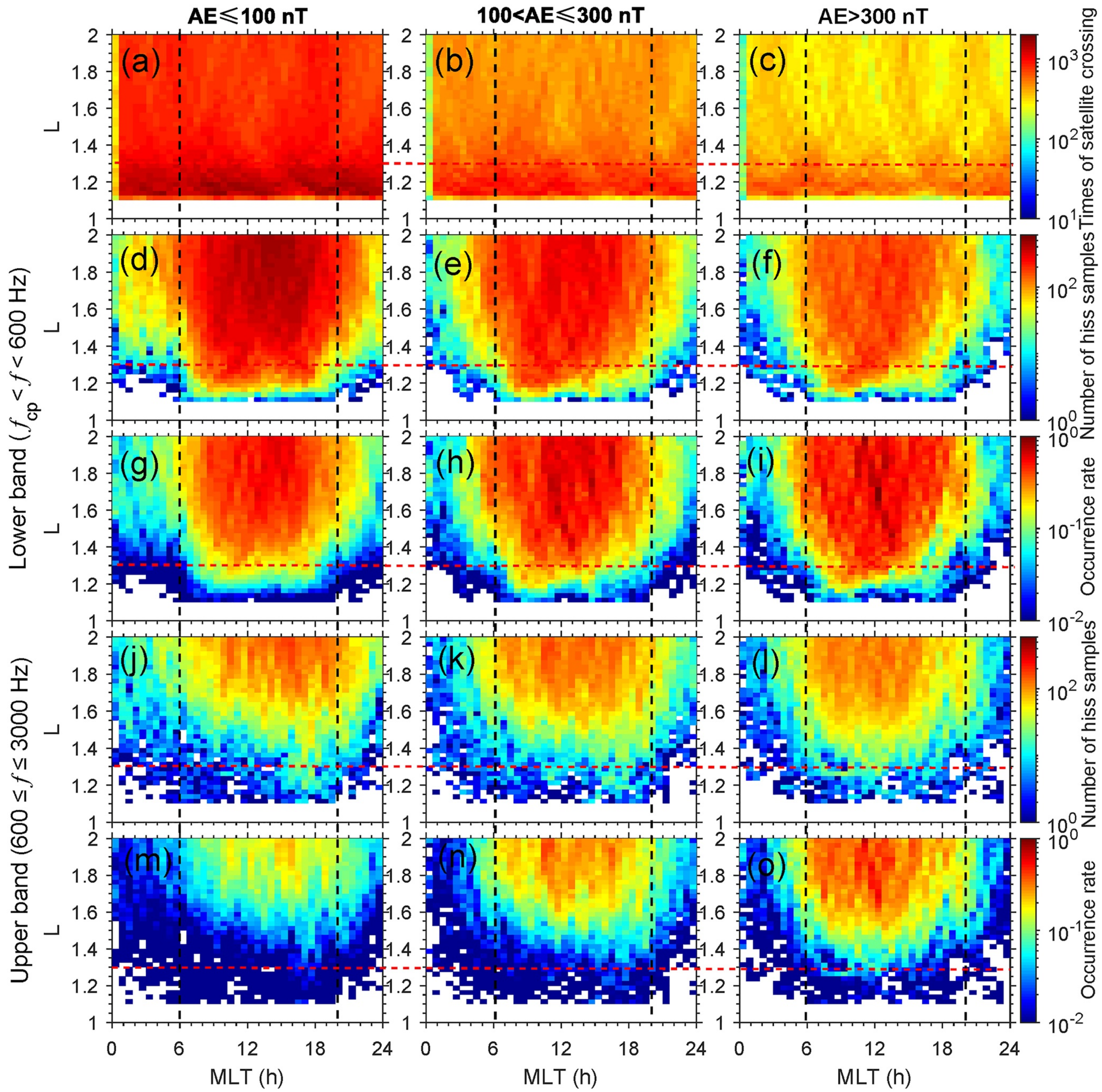

Figure 2. (a–c) Total number of times of the Van Allen Probes A and B passing through the inner belt region ($1.1 < L \leq 2$) during the statistical period (1 January 2013 to 28 February 2018). (d–i) The sample number and occurrence rate of lower-band hiss waves (<600 Hz). (j–o) The sample number and occurrence rate of upper-band hiss waves (≥600 Hz).

spatial variations and different substorm dependences indicate that the lower- and upper-band hiss waves come from different source regions. Potential wave sources are discussed in Section 4.

The stochastic frequency-spectrum distribution of the upper-band hiss waves cannot be fitted well with a fixed function, whereas the substorm-dependent power distribution of the lower-band hiss waves can be fitted with different Gaussian distributions, as indicated by the solid (observed values) and dashed curves (fitted values) in Figures 3c and 3d. The fitting functions are expressed as Equation 1, and the fitting parameters are listed in Table 1.

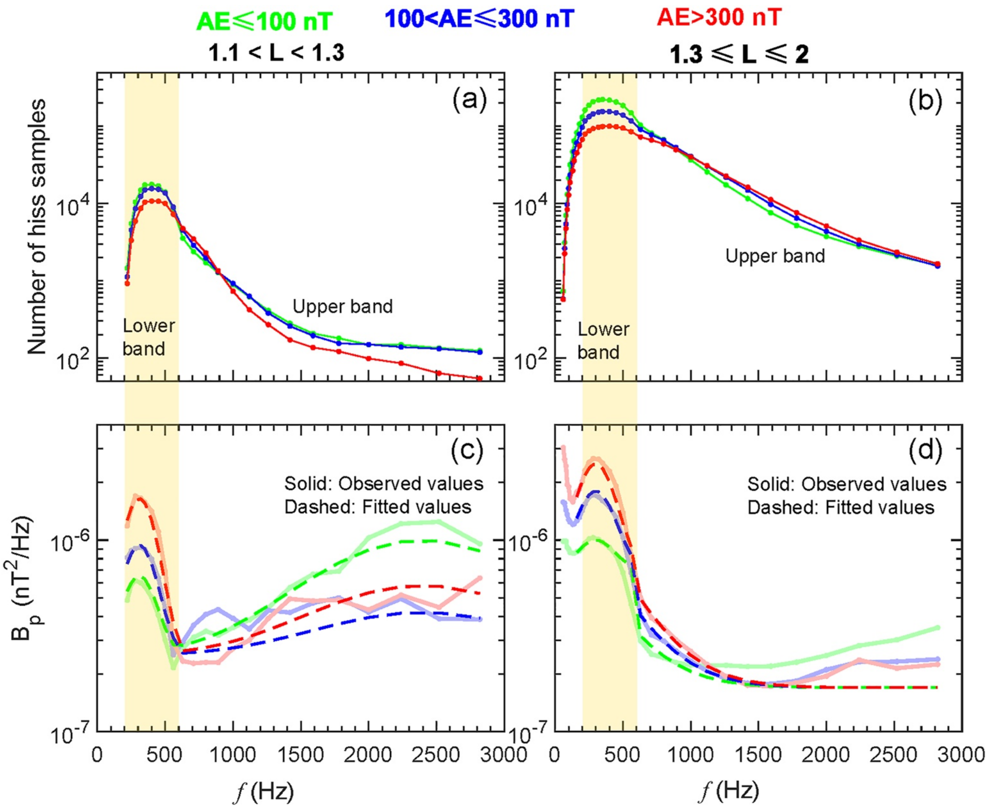

Figure 3. Hiss sample number and power spectral density VS frequency. Vertical shades roughly mark out the maximum sample number and peak power of the lower-band hiss waves (<600 Hz), while the frequency of the upper-band hiss waves is higher than 600 Hz.

$$B_p(f) = A\exp^{-\left(\frac{f-f_{\text{peak}}}{\Delta f}\right)^2} + B \tag{1}$$

where B_p is the power spectral density of wave magnetic field (nT^2/Hz). f is the wave frequency. f_{peak} and Δf are the peak power frequency and the frequency width, respectively. A and B are the fitting parameters.

Table 1
Fitted Parameters for the Frequency-Spectrum Distribution of Hiss Waves in the Inner Radiation Belt

		$f < 600$ Hz				$f \geq 600$ Hz			
Region (L in R_e)	AE index (nT)	A (10^{-7} nT^2/Hz)	f_{peak}	Δf	B($\times 10^{-7}$ nT^2/Hz)	A (10^{-7} nT^2/Hz)	f_{peak}	Δf	B (10^{-7} nT^2/Hz)
$1.1 < L < 1.3$	AE ≤ 100	4	310.0	160.0	2.5	7.5	2400.0	1,000.0	2.5
	100 < AE ≤ 300	6.7				1.7			
	AE > 300	14				3.3			
$1.3 \leq L \leq 2$	AE ≤ 100	3	300.0	180.0	7.0	500.0	2672.0	1,367.0	1.7
	100 < AE ≤ 300	11				800.0			
	AE > 300	18				1,100.0			

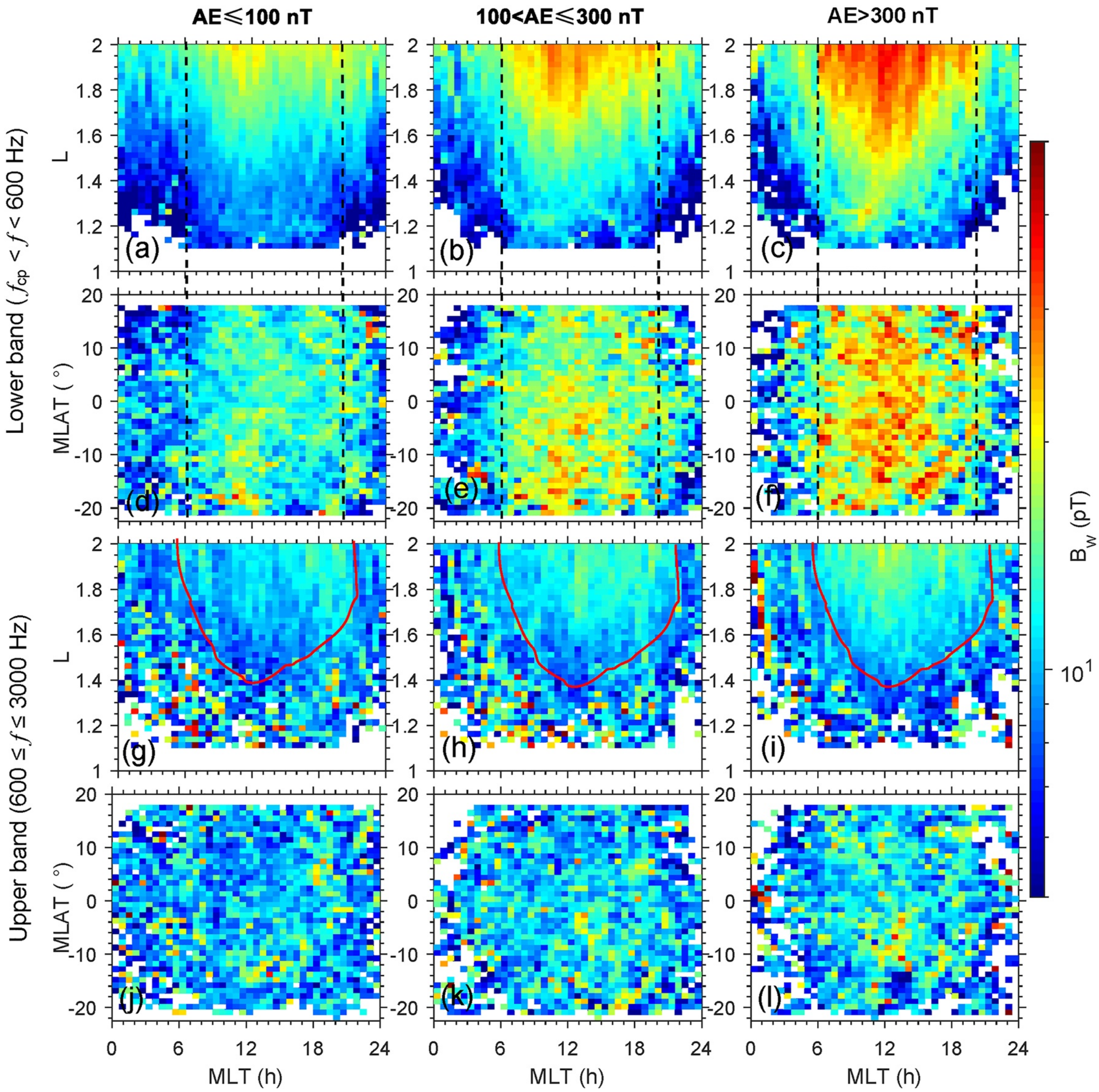

Figure 4. Spatial distributions of the amplitudes (B_w) of the lower- and upper-band hiss waves under different geomagnetic (AE) conditions. B_w is the statistical average of hiss wave amplitudes in each grid (0.6 MLT × 0.025 L) or (0.6MLT, 1.01MLAT).

3.2. Spatial Variations of Hiss Wave Amplitude and Propagation Angle

Figure 4 displays the L-MLT distributions of hiss wave amplitudes in the lower and upper bands under different geomagnetic conditions. The hiss amplitudes are averaged in each grid (0.6 MLT × 0.025 L) only considering the times when hiss waves are observed (i.e., amplitude > 0). The hiss amplitudes have significant radial variations but have no latitudinal difference. Like the power spectral densities, the amplitude (B_w) of the lower-band hiss is larger on the dayside than the nightside, and the dayside hiss amplitude increases as AE increases (Figures 4a–4f). Under the same AE level, the amplitude of the lower-band hiss decreases as L decreases. On the contrary, the larger amplitude upper-band hiss waves (≥600 Hz) mostly appear in the low-L region (below the V-shape curve in Figures 4g–4i) and they also extend into the high-L region ($L > 1.3$) on the nightside (MLT ∼ 20–6 hr). Except for the weak substorm dependence in the dayside high-L region, the amplitude of the upper-band hiss in other regions is nearly independent of substorm activities (AE). These differences suggest that the upper-band hiss waves in different regions have different sources.

The effect of substorm intensity (AE) on the different-band hiss waves is quantitatively evaluated in Figure 5. The hiss wave amplitudes under different AE levels are plotted as different color histograms and its relative change

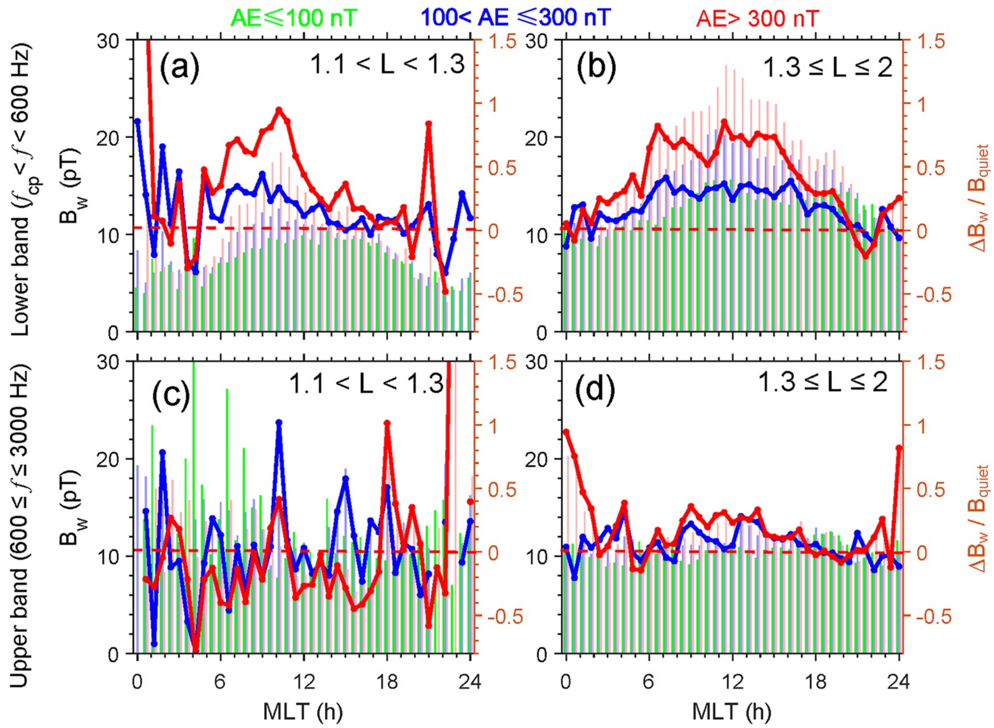

Figure 5. Hiss wave amplitude (histogram) and relative change rate (solid curves) under different geomagnetic (AE) conditions. (a) and (b) Lower-band hiss waves (<600 Hz). (c) and (d) Upper-band hiss waves (≥600 Hz).

rates $\left(\Delta B_w / B_{\text{quiet}} = B_{\text{quiet}} - B_{\text{active}} / B_{\text{quiet}}\right)$ are plotted as blue and red solid curves, respectively. As indicated by Figures 5a and 5b, as substorm activities are enhanced (AE increases), the amplitude of the lower-band hiss waves increases remarkably in the morning-side low-L region ($L < 1.3$ and MLT ∼ 6–12 hr) and in the entire dayside high-L region (MLT ∼ 6–20 hr and $L > 1.3$, where $\Delta B_w / B_{\text{quiet}} > 0$). This is consistent with the color panels in Figures 4a–4f. The relative change rate of the lower-band hiss amplitudes can exceed 50% during intense substorm activities (AE > 300 nT). However, the amplitude of the upper-band hiss waves has no regular variation during different substorm activities (Figures 5c and 5d), and the average change rate at all MLTs is nearly equal to zero.

Figure 6 displays the radial (L) and latitudinal (MLAT) distributions of the wave normal angle (WNA) and Poynting vector (polar angle θ) of the dayside and nightside hiss waves. Near the inner boundary ($L < 1.3$), the propagation directions of most hiss waves in the two bands are very oblique relative to the ambient magnetic field (WNA > 40°), and they can propagate toward the magnetic equator ($\theta > 90°$ for MLAT > 0° and $\theta < 90°$ for MLAT < 0°) or away from the magnetic equator ($\theta < 90°$ for MLAT > 0° and $\theta > 90°$ for MLAT < 0°) or along the azimuthal or radial directions ($\theta \sim 90°$). However, in the high-L region ($L > 1.3$), the WNAs of the lower- and upper-band hiss waves gradually decrease as MLAT decreases, and the nightside WNAs (Figures 6b and 6f) are generally larger than the dayside at the same L-MLAT location (Figures 6a and 6e). Interestingly, both the lower- and upper-band hiss waves at middle latitudes (|MLAT| > 10°) propagate toward the magnetic equator in the high-L region but their propagations are along azimuthal or radial directions at low latitudes (|MLAT| ≤ 10°).

4. Discussions

The equatorward propagation of the middle-latitude hiss waves suggests that most of the inner belt hiss waves come from high latitudes (|MLAT| > 22.4°). Previous ray tracings indicate that outer plasmaspheric hiss (Chen et al., 2017; Zhima et al., 2017) and lightning generated whistlers (LGWs) (Santolík et al., 2009) can propagate along magnetic field lines to high latitudes and then are refracted inwardly or outwardly. Therefore, outer plasmaspheric hiss and LGWs are two potential sources of the inner belt hiss waves but their contributions are perhaps different in different-L regions.

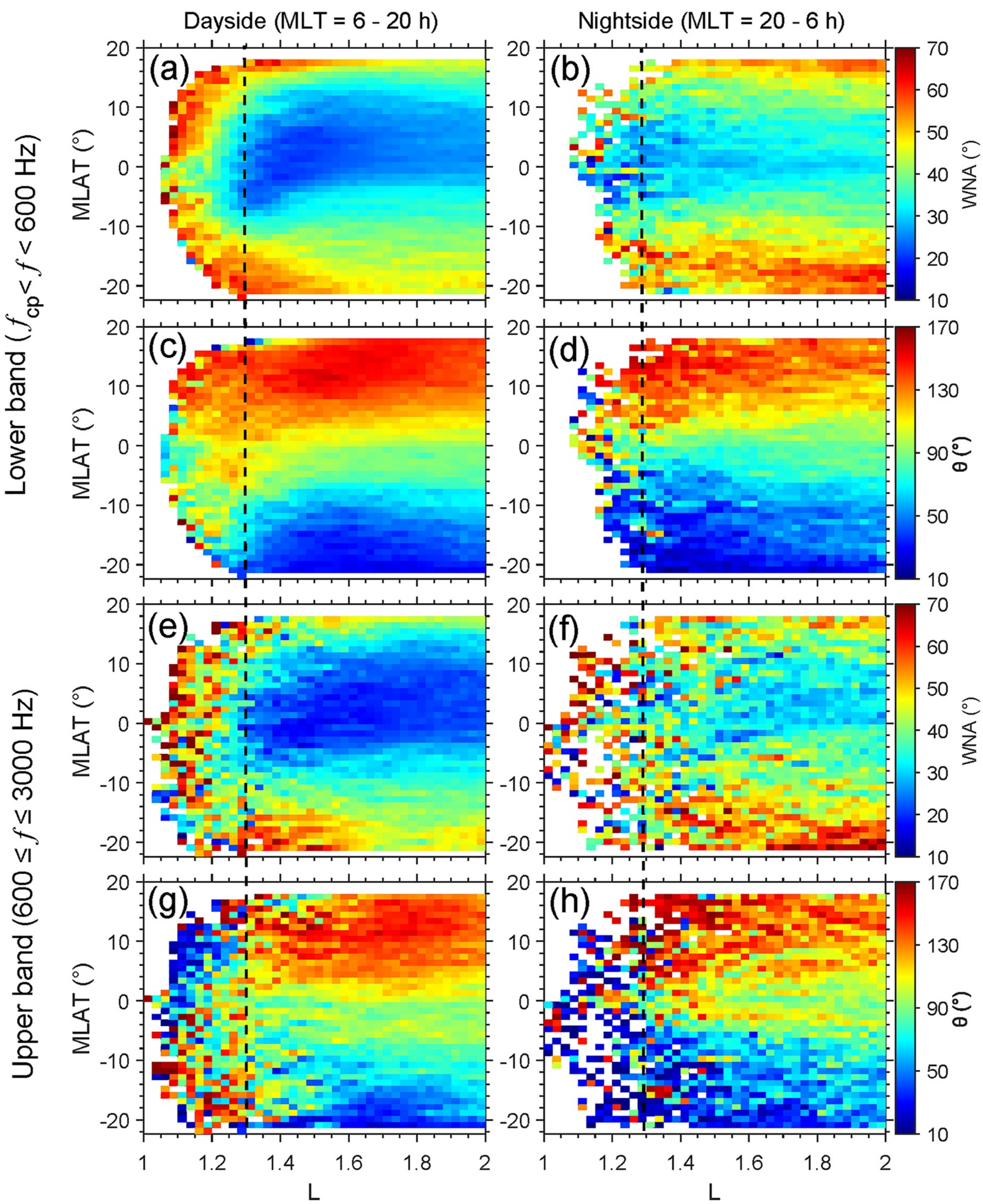

Figure 6. The radial (L) and latitudinal (MLAT) variations of hiss wave normal angles (WNA) and Poynting vector (polar angle θ) in the inner radiation belt ($1.1 < L < 2$). WNA and θ are their statistical medians in each grid (0.025 L and 1.01MLAT), respectively.

The frequency of the upper-band hiss waves ($f \geq 600$ Hz) is overlapped with the lower band of LGWs (Záhlava et al., 2019). The averaged power spectral density of the upper-band hiss waves in the high-L region ($L > 1.3$) is less than that near the inner boundary ($L < 1.3$) (Figures 3c and 3d). This is consistent with the power decay of upward propagating LGWs with propagation distance (see Figure 1a in Záhlava et al., 2019). In the left panels of Figure 1, the sporadic power enhancements are similar to the power spectral shapes of LGWs (Green et al., 2020). Since the upward propagating LGWs experience stronger ionospheric damping on the dayside than the nightside (Ripoll et al., 2020), the amplitude of the upper-band hiss waves in the nightside high-L region ($L > 1.3$) is larger than the dayside (Figures 4g–4i). The day-night asymmetry of the upper-band hiss amplitude in the high-L region is also consistent with that of the LGW powers (Green et al., 2020). The larger hiss amplitudes in the Low-L

region (L < 1.3) suggest that LGWs mainly contribute to the upper-band hiss waves near the inner boundary of the inner radiation belt. Since LGWs rely strongly on the seasonal lightning strokes in the lower atmosphere (Ripoll et al., 2020), the power and amplitude of the upper-band hiss waves have no obvious substorm dependence in Figures 3–5.

Of course, LGWs are not the only source of the upper-band hiss waves in the inner radiation belt. In the dayside high-L region (L > 1.3 and MLT = 6–20 hr), the weak substorm dependence of the amplitude of the upper-band hiss waves (Figures 4g–4i) is similar to that of outer plasmaspheric hiss in the region of L > 2 (Meredith et al., 2004, 2007; Yu et al., 2017), suggesting that some of the upper-band hiss waves also originate from the outer plasmaspheric hiss. In the right panels of Figure 1, the continuous power spectral density at high frequencies (>600 Hz) is different from the separated stripes of LGWs reported by Green et al. (2020). In our statistical results (Figures 2–6), the upper-band hiss waves originating from outer plasmaspheric hiss are not separated from those coming from LGWs. Thus, the occurrence rate of the mixing upper-band hiss waves is higher in the dayside high-L region than the nightside (Figures 2m–2o). This is different from the occurrence rate distribution of the pure LGWs reported by Green et al. (2020).

In contrast to the mixing upper-band hiss waves from multiple sources, the power and amplitude of the lower-band hiss waves have more significant substorm dependence and day-night asymmetry in the inner radiation belt. These properties are very similar to those of outer plasmaspheric hiss (L > 2) (Meredith et al., 2004, 2007; Yu et al., 2017). Comparing the lower-band hiss waves (f < 600 Hz in Figures 3c and 3d) with the outer plasmaspheric hiss (Figure 2 in Meredith et al. (2007) and Figure 2b in Spasojevic et al. (2015)), it can be found that their peak powers are distributed nearly in the same band (~200–500 Hz). These pieces of key evidence support that the outer plasmaspheric hiss is a dominant source of the low-band hiss waves in the inner radiation belt. From the high-L to low-L region, the amplitude decay of the lower-band hiss waves (<600 Hz) also agrees with the dissipation of wave energy with propagation distance (Liu et al., 2020).

In the high-L region (L > 1.3), the latitudinal variations of the WNAs of the upper- and lower-band hiss waves (Figure 6) are nearly the same as the outer plasmaspheric hiss (Agapitov et al., 2013; Yu et al., 2017). However, in the low-L region (L < 1.3), the WNA of the upper-band hiss waves (dayside median ~ 41.9° and nightside median ~ 45.4°) is comparable to that of LGWs in the region of L < 2 (Green et al., 2020). The inner belt hiss waves with different WNAs could result in the different diffusion rates of the radiation belt electrons as suggested by previous simulations (Gao et al., 2015). We will use the statistical model of the inner belt hiss to simulate wave-particle interactions in the future.

5. Summary and Conclusions

Based on the Van Allen Probes A and B observations for more than 5 years, we obtained the occurrence rate, amplitude, propagation angle, and frequency-spectrum distribution of the inner belt hiss waves under different geomagnetic conditions. We found that the intense lower-band hiss waves (<600 Hz) mostly appear in the dayside high-L region (L > 1.3 and MLT = 6–20 hr), whereas the intense upper-band hiss waves (≥600 Hz) mostly appear in the dayside low-L region (L < 1.3) and most nightside regions (MLT ~ 20–6 hr). Like the outer plasmaspheric hiss (L > 2), the amplitude of the lower-band hiss increases with enhanced substorm activities (AE increases), and their peak power spectral densities are located nearly in the same band (~200–500 Hz). The equatorward propagation of middle-latitude hiss suggests that the lower-band hiss waves in the inner radiation belt mostly originate from the outer plasmaspheric hiss at high latitudes.

Although the outer plasmaspheric hiss is also a likely source of the weak upper-band hiss (≥600 Hz) in the dayside high-L region (L > 1.3 and MLT = 6–20 hr), the amplitude of the intense upper-band hiss has no obvious substorm dependence in the dayside low-L region and most night regions. In the low-L region, the averaged wave normal angle of the upper-band hiss is comparable to that of LGWs reported in the past. These results suggest that LGWs are the dominant source of upper-band hiss near the inner boundary of the inner radiation belt.

Data Availability Statement

The EMFISIS data of Van Allen Probes are publicly available at the Web https://emfisis.physics.uiowa.edu/. The AE index is publicly available from the OMNI database at the CDAWeb http://cdaweb.gsfc.nasa.gov/sp_phys.

Acknowledgments
This work is supported by the National Natural Science Foundation of China (41821003, 41874192, and 41374165). We thank the EMFISIS group for wave data we also thank other staff for the AE index.

References

Agapitov, O. V., Artemyev, A., Krasnoselskikh, V., Khotyaintsev, Y. V., Mourenas, D., Breuillard, H., et al. (2013). Statistics of whistler mode waves in the outer radiation belt: Cluster STAFF-SA measurements. *Journal of Geophysical Research*, *118*(6), 3407–3420. https://doi.org/10.1002/jgra.50312

Cao, J. B., Liu, Z. X., Yang, J. Y., Yian, C. X., Wang, Z. G., Zhang, X. H., et al. (2005). First results of low frequency electromagnetic wave detector of TC-2/Double Star program. *Annales Geophysicae*, *23*(8), 2803–2811. https://doi.org/10.5194/angeo-23-2803-2005

Chen, L., Santolík, O., Hajoš, M., Zheng, L., Zhima, Z., Heelis, R., et al. (2017). Source of the low-altitude hiss in the ionosphere. *Geophysical Research Letters*, *44*(5), 2060–2069. https://doi.org/10.1002/2016GL072181

Gao, Y., Xiao, F., Yan, Q., Yang, C., Liu, S., He, Y., & Zhou, Q. (2015). Influence of wave normal angles on hiss-electron interaction in Earth's slot region. *Journal of Geophysical Research: Space Physics*, *120*, 9385–9400. https://doi.org/10.1002/2015JA021786

Green, A., Li, W., Ma, Q., Shen, X.-C., Bortnik, J., & Hospodarsky, G. B. (2020). Properties of lightning generated whistlers based on Van Allen Probes observations and their global effects on radiation belt electron loss. *Geophysical Research Letters*, *47*(17), e2020GL089584. https://doi.org/10.1029/2020GL089584

Kletzing, C. A., Kurth, W. S., Acuna, M., MacDowall, R. J., Torbert, R. B., Averkamp, T., et al. (2013). The electric and magnetic field instrument suite and integrated science (EMFISIS) on RBSP. *Space Science Reviews*, *179*(1–4), 127–181. https://doi.org/10.1007/s11214-013-9993-6

Li, L. Y., Cao, J. B., & Zhou, G. C. (2006). Relation between the variation of geomagnetospheric relativistic electron flux and storm/substorm. *Chinese Journal of Geophysics*, *49*, 9–15. https://doi.org/10.1002/cjg2.805

Li, L. Y., Cao, J. B., & Zhou, G. C. (2008). Whistler-mode waves modify the high-energy electron slot region and the outer radiation belt. *Chinese Journal of Geophysics*, *51*(2), 316–324. https://doi.org/10.1002/cjg2.1213

Li, L. Y., Cao, J. B., Zhou, G. C., & Li, X. (2009). Statistical roles of storms and substorms in changing the entire outer zone relativistic electron population. *Journal of Geophysical Research*, *114*(A12), A12214. https://doi.org/10.1029/2009JA014333

Li, L. Y., & Wang, Z. Q. (2018). The effects of solar wind dynamic pressure changes on the substorm auroras and energetic electron injections on 24 August 2005. *Journal of Geophysical Research: Space Physics*, *123*(1), 385–399. https://doi.org/10.1002/2017JA024628

Li, L. Y., Wang, Z. Y., Yu, J., & Cao, J. B. (2021). Complementary and catalytic roles of man-made VLF waves and natural plasma waves in the loss of radiation belt electrons. *Journal of Geophysical Research: Space Physics*, *126*(10), e2020JA028879. https://doi.org/10.1029/2020JA028879

Li, L. Y., Yang, S. S., Cao, J. B., Yu, J., Luo, X. Y., & Blake, J. B. (2019). Effects of solar wind plasma flow and interplanetary magnetic field on the spatial structure of earth's radiation belts. *Journal of Geophysical Research: Space Physics*, *124*, 10332–10344. https://doi.org/10.1029/2019JA027284

Li, L. Y., Yu, J., Cao, J. B., Chen, L. J., Reeves, G. D., & Blake, J. B. (2022). Competitive influences of different plasma waves on the pitch angle distribution of energetic electrons inside and outside plasmasphere. *Geophysical Research Letters*, *49*(1), e2021GL096062. https://doi.org/10.1029/2021GL096062

Li, L. Y., Yu, J., Cao, J. B., Yang, J. Y., Li, X., Baker, D. N., et al. (2017). Roles of whistler mode waves and magnetosonic waves in changing the outer radiation belt and the slot region. *Journal of Geophysical Research: Space Physics*, *122*(5), 5431–5448. https://doi.org/10.1002/2016JA023634

Li, W., Ma, Q., Thorne, R. M., Bortnik, J., Kletzing, C. A., Kurth, W. S., et al. (2015). Statistical properties of plasmaspheric hiss derived from Van Allen Probes data and their effects on radiation belt electron dynamics. *Journal of Geophysical Research: Space Physics*, *120*(5), 3393–3405. https://doi.org/10.1002/2015JA021048

Liu, N., Su, Z., Gao, Z., Zheng, H., Wang, Y., Wang, S., et al. (2020). Comprehensive observations of substorm-enhanced plasmaspheric hiss: Generation, propagation, and dissipation. *Geophysical Research Letters*, *47*(2), e2019GL086040. https://doi.org/10.1029/2019GL086040

Lyons, L. R., & Thorne, R. M. (1973). Equilibrium structure of radiation belt electrons. *Journal of Geophysical Research*, *78*(13), 2142–2149. https://doi.org/10.1029/JA078i013p02142

Meredith, N. P., Horne, R. B., Glauert, S. A., & Anderson, R. R. (2007). Slot region electron loss timescales due to plasmaspheric hiss and lightning-generated whistlers. *Journal of Geophysical Research*, *112*(A8), A08214. https://doi.org/10.1029/2007JA012413

Meredith, N. P., Horne, R. B., Kersten, T., Li, W., Bortnik, J., Sicard, A., & Yearby, K. H. (2018). Global model of plasmaspheric hiss from multiple satellite observations. *Journal of Geophysical Research: Space Physics*, *123*(6), 4526–4541. https://doi.org/10.1029/2018JA025226

Meredith, N. P., Horne, R. B., Thorne, R. M., Summers, D., & Anderson, R. R. (2004). Substorm dependence of plasmaspheric hiss. *Journal of Geophysical Research*, *109*(A6), A06209. https://doi.org/10.1029/2004JA010387

Ripoll, J.-F., Farges, T., Malaspina, D. M., Lay, E. H., Cunningham, G. S., Hospodarsky, G. B., et al. (2020). Analysis of electric and magnetic lightning-generated wave amplitudes measured by the Van Allen Probes. *Geophysical Research Letters*, *47*(6), e2020GL087503. https://doi.org/10.1029/2020GL087503

Santolík, O., Pickett, J. S., Gurnett, D. A., Menietti, J. D., Tsurutani, B. T., & Verkhoglyadova, O. (2010). Survey of Poynting flux of whistler mode chorus in the outer zone. *Journal of Geophysical Research*, *115*(A7), A00F13. https://doi.org/10.1029/2009JA014925

Santolík, O., & Parrot, M. (1999). Case studies on the wave propagation and polarization of ELF emissions observed by Freja around the local proton gyrofrequency. *Journal of Geophysical Research*, *104*(A2), 2459–2475. https://doi.org/10.1029/1998JA900045

Santolík, O., Parrot, M., Inan, U. S., Buresˇova, D., Gurnett, D. A., & Chum, J. (2009). Propagation of unducted whistlers from their source lightning: A case study. *Journal of Geophysical Research*, *114*, A03212. https://doi.org/10.1029/2008JA013776

Santolík, O., Parrot, M., & Lefeuvre, F. (2003). Singular value decomposition methods for wave propagation analysis. *Radio Science*, *38*(1), 1010. https://doi.org/10.1029/2000RS002523

Spasojevic, M., Shprits, Y. Y., & Orlova, K. (2015). Global empirical models of plasmaspheric hiss using Van Allen Probes. *Journal of Geophysical Research: Space Physics*, *120*, 10370–10383. https://doi.org/10.1002/2015JA021803

Su, Z., Liu, N., Zheng, H., Wang, Y., & Wang, S. (2018). Large-amplitude extremely low frequency hiss waves in plasmaspheric plumes. *Geophysical Research Letters*, *45*(2), 565–577. https://doi.org/10.1002/2017GL076754

Thorne, R. M., Smith, E. J., Burton, R. K., & Holzer, R. E. (1973). Plasmaspheric hiss. *Journal of Geophysical Research*, *78*(10), 1581–1596. https://doi.org/10.1029/JA078i010p01581

Wang, J. L., Li, L. Y., & Yu, J. (2020). Statistical relationship between exohiss waves and plasmaspheric hiss. *Geophysical Research Letters*, *47*(5), e2020GL087023. https://doi.org/10.1029/2020GL087023

Xia, Z., Chen, L., Zhima, Z., Santolik, O., Horne, R. B., & Parrot, M. (2019). Statistical characteristics of ionospheric hiss waves. *Geophysical Research Letters*, *46*(13), 7147–7156. https://doi.org/10.1029/2019GL083275

Yu, J., Li, L. Y., Cao, J. B., Chen, L., Wang, J., & Yang, J. (2017). Propagation characteristics of plasmaspheric hiss: Van Allen Probe observations and global empirical models. *Journal of Geophysical Research: Space Physics*, *122*(4), 4156–4167. https://doi.org/10.1002/2016JA023372

Yu, J., Li, L. Y., Cao, J. B., Yuan, Z. G., Reeves, G. D., Baker, D. N., et al. (2015). Multiple loss processes of relativistic electrons outside the heart of outer radiation belt during a storm sudden commencement. *Journal of Geophysical Research: Space Physics*, *120*, 10275–10288. https://doi.org/10.1002/2015JA021460

Yu, J., Wang, J., Li, L. Y., Cui, J., Cao, J. B., & He, Z. G. (2020). Electron diffusion by coexisting plasmaspheric hiss and chorus waves: Multisatellite observations and simulations. *Geophysical Research Letters*, *47*, e2020GL088753. https://doi.org/10.1029/2020GL088753

Záhlava, J., Němec, F., Santolík, O., Kolmašová, I., Hospodarsky, G. B., Parrot, M., et al. (2019). Lightning contribution to overall whistler mode wave intensities in the plasmasphere. *Geophysical Research Letters*, *46*, 8607–8616. https://doi.org/10.1029/2019GL083918

Zhima, Z., Chen, L., Xiong, Y., Cao, J., & Fu, H. (2017). On the origin of ionospheric hiss: A conjugate observation. *Journal of Geophysical Research: Space Physics*, *122*, 11784–11793. https://doi.org/10.1002/2017JA024803